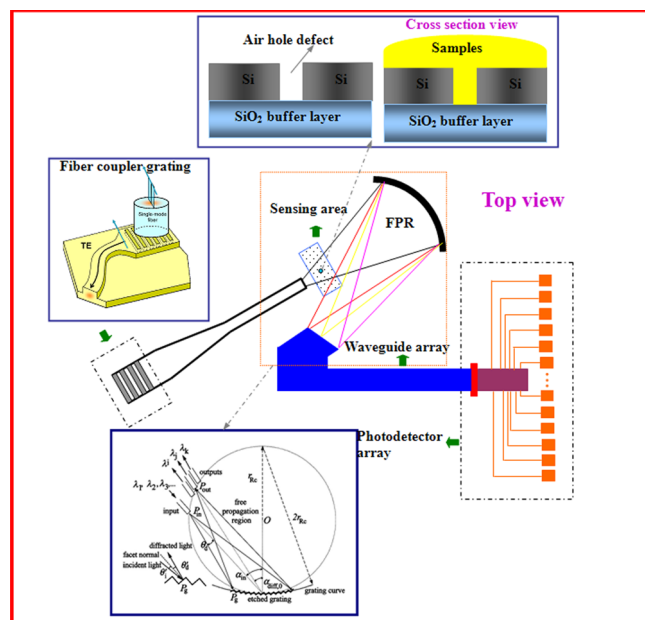# A Highly Sensitive Optical Sensor Design by Integrating a Circular-Hole Defect With an Etched Diffraction Grating Spectrometer on an Amorphous-Silicon Photonic Chip

J. Song
Y. Z. Li
X. Zhou
X. Li

A Highly Sensitive Optical Sensor Design by Integrating a Circular-Hole Defect With an Etched Diffraction Grating Spectrometer on an Amorphous-Silicon Photonic Chip

J. Song,[1] **Y. Z. Li,**[1] **X. Zhou,**[1] **and X. Li**[2]

[1]Institute of Optoelectronics, Key Lab of Optoelectronics Devices and Systems of Ministry of Education/Guangdong Province, Shenzhen University, Shenzhen 518060, China
[2]Science College, Hangzhou Normal University, Hangzhou 310036, China

Abstract: We present a sensitive optical sensor design by integrating a circular-hole defect with an etched diffraction grating (EDG) spectrometer based on amorphous-silicon photonic platforms. The circular-hole defect obtained from the outdiffusion of the hydrogen in the annealing process can induce strong resonant scattering loss at some special wavelengths. The positions of resonant peaks will linearly shift with the refractive index change of the detected sample (the sensitivity is ~9200 nm/RIU). In addition, the influences of the defect on the sensing characteristics are numerically analyzed based on a scalar diffraction method and a Green tensor technology.

Index Terms: Sensors, silicon nanophotonics.

1. Introduction

Planar waveguide-based optical sensors have received great attention for their applications in many areas, such as biological sensing, environmental monitoring, and chemical analysis. Different technologies based on different materials have been introduced to support planar waveguide sensors. Waveguides usually induce reactions at the surface within the evanescent field and can efficiently convert the refractive index change caused by detected samples to a measurable spectral shift in their optical transmissions. Recently, high-refractive-index silicon-on-insulator (SOI) optical sensing platforms in various extensions have been developed with the advantage of the high sensitivity [1]–[5]. Above all, SOI based sensors using microcavity structures have widely been used because of the sharp resonance peak and their ultracompact sizes [6]–[10].

Optical waveguide sensors have to fulfill very sensitive, stable, and reliable detection requirements. For a typical planar waveguide sensor, the refractive index change from the detected sample can typically be derived from the wavelength shift of the functional signal by using a spectrometer. However, conventional spectrometers are large and expensive and have a performance that often exceeds the requirements for optical sensing applications. Therefore, it is very cost effective to design and fabricate planar waveguide sensors with an integrated spectrometer on a chip.
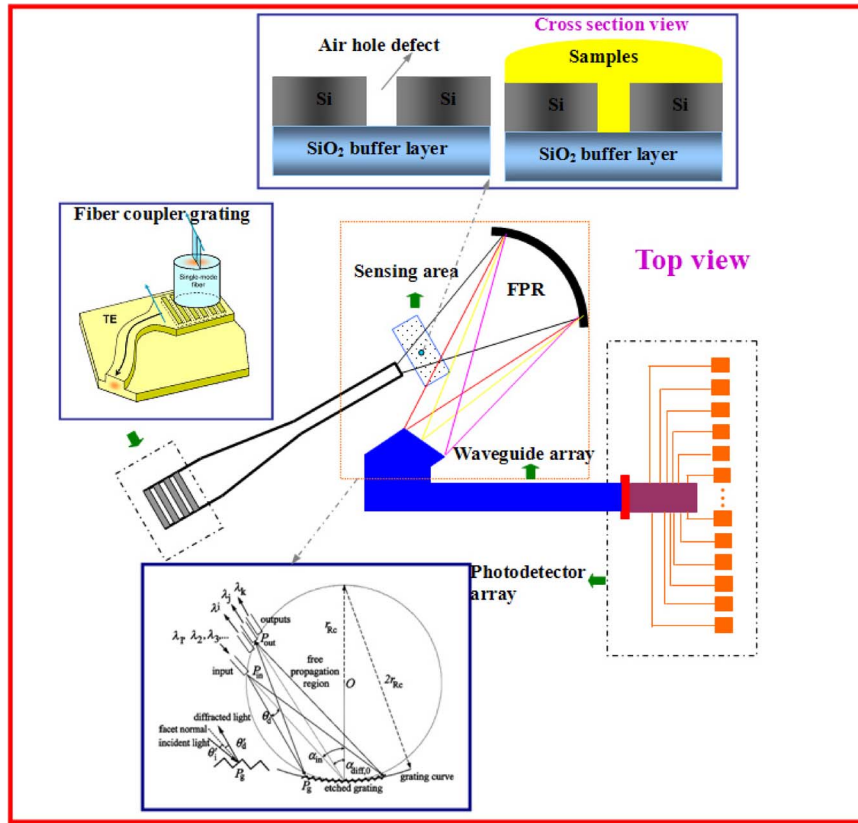
Fig. 1. Schematic configuration of proposed optical sensor by integrating a circular-hole defect with an EDG spectrometer.

Recently, we have proposed a gas sensor based on the resonant scattering effect of a small defect in SOI waveguides at some special operating wavelengths, which exhibits very high sensitivity [11]. Now, we will integrate a similar defect with an etched diffraction grating (EDG) spectrometer on the same chip using the amorphous-silicon platform [12]–[14] and apply the device into optical sensors. However, the small defect in the previous works is produced in random in the process of waveguide deposition. Now, we present a method to fabricate circular-hole defects using an annealing process. Moreover, the circular-hole defect is integrated with an EDG, which works as a wavelength filter (i.e., integrated spectrometer) to measure the position change of the resonant loss peak.

2. Designs, Fabrications and Measurements

In the present paper, we will design and fabricate a planar waveguide chip able to sense the refractive index change of the detected sample by integrating a circular-hole defect with an EDG spectrometer. The planar sensor based on an SOI structure has ~ 5 μm silica buffer layer, which is thick enough to ensure a low leakage loss. The thickness of the waveguide core layer equals 250 nm, and the width for single mode input and output waveguides is chosen as 500 nm. The layers of SiO_2 and α-Si are deposited in sequence with the technology of plasma-enhanced chemical vapor deposition (PECVD).

The schematic configuration presented in Fig. 1 is a view of the sensor. The proposed chip consists of a fiber coupler, an EDG, a sensing area with a circular-hole defect, and arrayed photodectors heterogeneously integrated on top of the output silicon waveguides. Light is first coupled from a fiber

to the chip via a planar grating coupler. An input single mode fiber is aligned and glued on the top of the fiber coupler using ultraviolet-curable glue. An amplified spontaneous emission (ASE) source gives a broadband unpolarized light with spectral range 1530 nm–1580 nm. This unpolarized light is butt-coupled to the single mode fiber through a focusing gradient index lens. The light is guided trough the input waveguide and crosses the sensing area with a circular-hole defect. Next, the light is guided to the EDG spectrometer which separates and focused the light into 16 different wavelength channels. Finally, 16 InGaAs photodetectors can be integrated on top of the 16 output waveguides to measure the optical power in the 16 different wavelength channels.

A typical EDG is based on a Rowland mounting. The field propagating from an input waveguide to the free propagation region (FPR) is diffracted by each grating facet. It is then refocused onto an imaging curve and guided into the corresponding output waveguides according to the wavelengths. The circular-hole defect close to the input waveguide (i.e., the sensing area in Fig. 1) can influence the distribution of the input field. We have shown that the defect with some special shapes and indices can produce strong resonances with the incident light, and then little power can be coupled into the corresponding output waveguide. The resonant wavelength is very sensitive to the refractive index change of detected samples [11]. The position of the resonant peak can be detected using the arrayed photodetectors in Fig. 1.

However, in the paper, we do not integrate the arrayed photodetectors, but only connect each output port of the EDG with a power meter with $\sim\pm2$ nW resolution to measure the transmission power at the corresponding wavelength. In the future, InGaAs metal–semiconductor–metal (MSM) photodetectors can be heterogeneously integrated on top of the output waveguides of the EDG in order to contribute to a much better stability [15].

Owing to the large index contrast of the amorphous-silicon waveguide, EDG devices can be made very compact. Moreover, they can be manufactured on high-quality wafers using standard CMOS fabrication tools, making these devices cheap for the market. In the recent years, we and other research groups have demonstrated variable EDG designs and fabrications based on the silicon nanophotonic platform, which is a promising material system for a wide range of applications, such as telecommunications and optical sensors [16]–[21].

The EDG spectrometer in the sensing device has the following parameters: The central wavelength is 1550 nm; the refractive indices of silica buffer layer and α-Si:H core layer are 1.46 and 3.58, respectively; the incident angle is 45°; the diffraction order is 6; the grating period is ~1.6 μm; the number of the grating groove is ~120; the channel interval is 1.6 nm; and the internal of output waveguides is 5 μm.

As the beginning step of the whole device fabrication, a 5-μm silica buffer layer (i.e., SiO$_2$) and a 220-nm α-Si:H core layer are successively deposited on a silicon wafer. Then, a process of pattern generation will be carried out using lithography technology with high resolution and accuracy. In the paper, the electron beam lithography based on negative resists is employed due to its low running cost and ability to push the resolution further down to 50 nm. Fig. 2 gives some pictures of the fabricated device (i.e., the region with the dotted square in Fig. 1). To increase the coupling efficiency, the width of each input and output waveguide is tapered from 500 nm to 2 μm through a linear taper (see enlarged picture at the upper-right corner in Fig. 2). The circular defect close to the input waveguide is an air hole and has a ~1-μm diameter (see enlarged picture at the middle-upper direction in Fig. 2). Although EDGs using silicon nanowire technology have compact structure, the large polarization dependence which makes that a device such as a spectrometer can be only utilized for one polarization state without any compensation. In the present paper, only TE polarization is considered as an example to clarify our design.

In the previous works, the small defects are produced in random in the process of waveguide deposition. We cannot control their shapes and numbers [11]. In the present paper, we will fabricate special circular-hole defects on the surface of the amorphous-silicon layers deposited by PECVD technology based on the thermal annealing at temperatures above deposition temperatures.

The main parameters in the thermal annealing process are the temperature ramping rate, the maximum temperature and the holding time. We use a horizontal quartz tube oven with nitrogen atmosphere for the annealing process. The holding time at maximum temperature (i.e., 600 °C) is
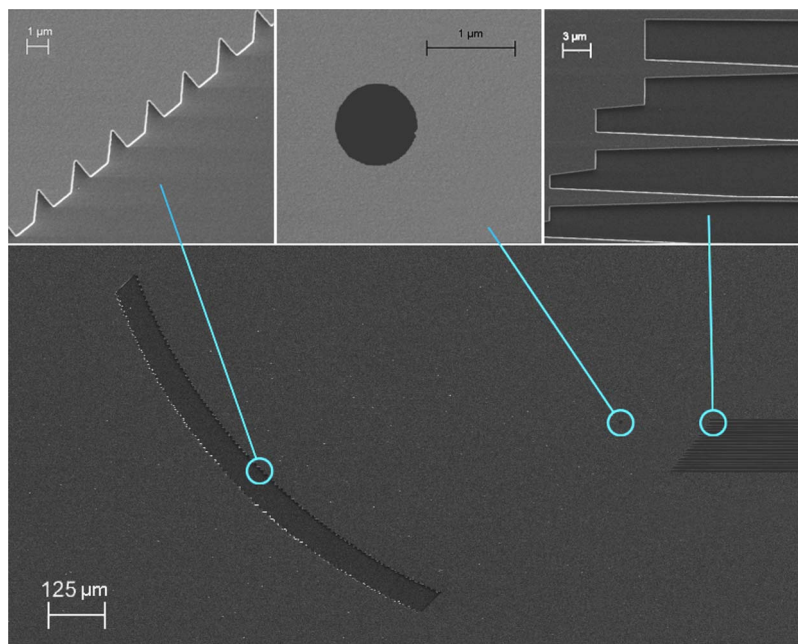
Fig. 2. Top-view SEM pictures of the fabricated device corresponding to the region with the dotted square in Fig. 1.

chosen as $\sim$10 min to achieve sufficient temperature stabilization. In the process, the outdiffusion of the hydrogen in the α-Si:H thin film will result in circular-hole defects on the surface. The number of defects per unit area rapidly increases as both the maximum temperature and the thickness of the thin film increase. Since the thickness of silicon waveguide is only 250 nm for the present application, it is relatively stable with the 600 °C maximum annealing temperature. Only several small circular-hole defects exist on the whole wafer. From Fig. 2, one can see that only one circular-hole defect with $\sim$1 μm diameter exists in the FPR of the EDG spectrometer.

In the paper, the fabricated device is measured from bulk sensing experiments with the NaCl solution. Using an Abbe refractometer, we have verified that there is a good linear relationship between the concentration ($c\%$) and the refractive index (n) for the NaCl solution at 20 °C, i.e., $n = 1.3331 + 0.00185c\%$, which is consistent with some published works [10], [22]. The temperature is kept constant at 20 °C by means of a Peltier element connected to a temperature controller. We manually added a solution drop in the sensing box, and clean off the residue with the deionized water before a new measurement is carried out. When the sample is dropped into the sensing area, it not only fills the air circular-hole defect but covers parts of the silicon waveguide surface as well (see the cross-sectional view of the sensing area in Fig. 1). However, we have shown that the overflowing sample on the surface has no influence on the position of the resonant scattering peak but will induce some extra loss (maybe due to the absorption). We find that the position of the loss peak will shift toward a longer wavelength direction as the NaCl-solution concentration increases. Fig. 3 shows the detected transmission loss with a TE polarization for NaCl concentrations of 0.474, 0.859, and 1.248 mass% at 16 channels using the power meter.

Fig. 4 shows the resonant scattering wavelength as a function of the refractive index of the NaCl solution using the device. From this figure, one can see that the spectral position of the resonant scattering peak shifts linearly with the refractive index of the NaCl solution with a sensitivity as high as 9211 nm/RIU. When the transmission spectrum of the device is measured with a commercial optical spectrum analyzer (OSA) with resolution setting of 0.1 nm, we obtain the standard deviation of the noise on the signal to $\sim$35 pm by averaging it with a 3-min window, which corresponds to a detection limit of the device as high as $\sim$3.8 · 10^{-6} RIU. Note that the measurement is carried out
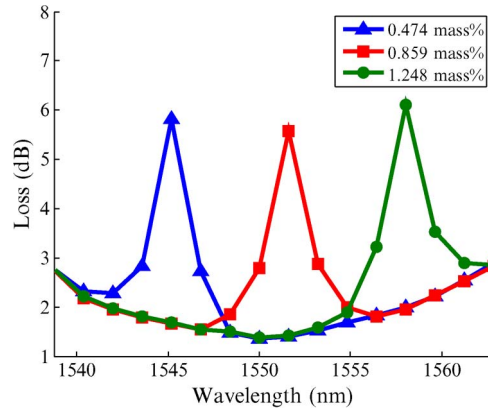
Fig. 3. Detected transmission loss at 16 channels of the EDG spectrometer for the NaCl solution with different concentrations.
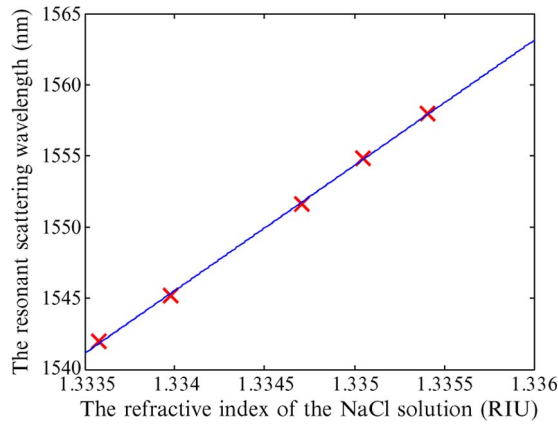

Fig. 4. Resonant scattering wavelength varies as a function of the refractive index of the NaCl solution for the optical sensor.

using a commercial OSA since the power meter cannot present enough wavelength resolution to achieve the measurement. Therefore, the actual detection limit of the refractive index may have a small difference compared with the present value depending on the stability of the power meter.

3. Simulations and Discussions

In this section, we will present a numerical model to furthermore accurately analyze the performance of the sensor device. If no point defect exists, the FPR is homogeneous (see Fig. 5). Owing to its simplicity, the scalar diffraction method is commonly used for the accurate simulation of the propagation of the incident light field in the FPR. Thus, the incident field E_0 at any point P in the calculation region "$ABCD$" can be calculated with an integral over the cross-sectional line "AB" where the end of the input waveguide is positioned (hereafter referred as the input plane)

$$E_0(x, z) = \frac{1}{2} \left(\frac{n_{\text{eff}}}{\lambda}\right)^{\frac{1}{2}} \cdot \int_{\text{input}} \frac{E_{\text{in}}(x', z')}{\sqrt{|P_{\text{in}}P|}} \cdot (1 + \cos\theta_{\text{d}}) \cdot \exp(-jk|P_{\text{in}}P|) \cdot dl' \tag{1}$$

where n_{eff} and k are the effective refractive index (for a planar waveguide structure) and wavenumber in the FPR, respectively, λ is the wavelength in a vacuum, E_{in} denotes the fundamental mode field of the input waveguide at the input plane, $|P_{in}P|$ is the distance between point $P(x, z)$ and a point
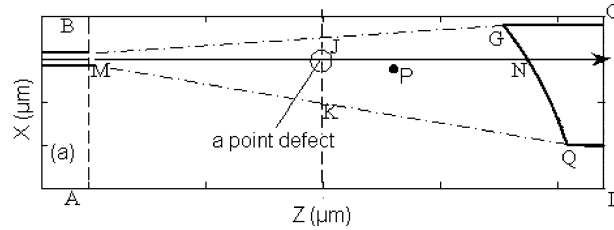
Fig. 5. Schematic diagram of a circular-hole defect in the FPR of an EDG spectrometer.

$P_{in}(x', z')$ on the input plane, and θ_d is the diffraction angle with respect to the normal of the input plane. When a point defect exists in the FPR (see Fig. 5), the field distribution $E(x, z)$ obeys the following Helmholtz's equation:

$$\nabla^2 E(x, z) - k_0^2 \varepsilon_w(x, z) E(x, z) = k_0^2 \Delta\varepsilon(x, z) E(x, z) \tag{2}$$

where $\varepsilon_w(x, z)$ and $\varepsilon(x, z)$ are the permittivity with or without point defect in the FPR, respectively. $\Delta\varepsilon(x, z)$ is defined as the difference of $\varepsilon(x, z)$ and $\varepsilon_w(x, z)$. The variety of the field due to the defect can be analyzed by Green functions method and the corresponding field distribution obeys Helmholtz's equation

$$\nabla^2 G(r, r_p) - k_0^2 \varepsilon_w(r, r_p) G(r, r_p) = \delta(r - r_p) \tag{3}$$

where r_p and r are any point in the region of the defect and the calculation region. Correspondingly, the total field in the waveguide with a defect can be expressed as

$$E(r) = E_0(r) - L\frac{\Delta\varepsilon(r)}{\varepsilon_w(r)}E(r) + \lim_{\delta V \to 0} \int_{V-\delta V} G(r, r_p) \cdot k_0^2 \Delta\varepsilon(r_p) E(r_p) \, dr_p \tag{4}$$

where L is a vector, and its value varies as the shape of the defect [23]. By using the method of moment [23], we convert (4) into a matrix equation

$$\begin{pmatrix} \ddots & \vdots & \vdots & \vdots & \\ \cdots & 1 - M_{i-1}\Delta\varepsilon_{i-1} & -G_{i-1,i}\Delta\varepsilon_i & -G_{i-1,i+1}\Delta\varepsilon_{i+1} & \cdots \\ \cdots & -G_{i,i-1}\Delta\varepsilon_{i-1} & 1 - M_i\Delta\varepsilon_i & -G_{i,i+1}\Delta\varepsilon_{i+1} & \cdots \\ \cdots & -G_{i+1,i-1}\Delta\varepsilon_{i-1} & -G_{i+1,i}\Delta\varepsilon_i & 1 - M_{i+1}\Delta\varepsilon_{i+1} & \cdots \\ & \vdots & \vdots & \vdots & \ddots \end{pmatrix}_{N_1 \times N_1} \begin{pmatrix} \vdots \\ E_{i-1} \\ E_i \\ E_{i+1} \\ \vdots \end{pmatrix}_{N_1} = \begin{pmatrix} \vdots \\ E_{i-1}^0 \\ E_i^0 \\ E_{i+1}^0 \\ \vdots \end{pmatrix} \tag{5}$$

where

$$M_i = k_0^2 \left[\frac{\sqrt{\pi \Delta x_i \Delta z_i}}{2k} H_1^{(1)}\left(k\sqrt{\frac{\Delta x_i \Delta z_i}{\pi}}\right) + \left(\frac{i}{k}\right)^2 \right]$$

$$G(r_i, r_q) = \frac{i}{4} k_0^2 H_0^{(1)}\left(k\sqrt{(x_i - x_q)^2 + (z_i - z_q)^2}\right)$$

which is of the simple form $A \cdot x = b$. For the present problem, since the area of the defect is very small relative to all computational regions, most elements of the matrix A are zero. Therefore, using a blocked matrix method, the large sparse matrix equation can be solved simply. Although N_1 is very large, the scattering field can be obtained within a few minutes on a personal computer. Once (5) is solved, the actual field distribution at any point P can be calculated. Particularly, one can obtain the incident field at any point P_g on the etched grating surface.
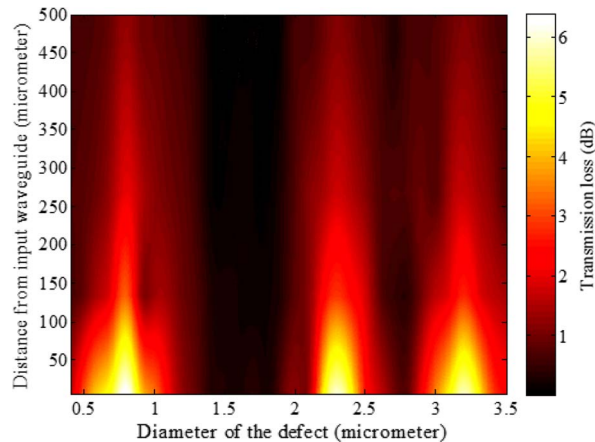
Fig. 6. Loss at variable positions and diameters of the circular-hole defect for an EDG spectrometer at the central wavelength.

When no point defect exists in the FPR, the diffraction field at any point P in the calculation region given in Fig. 5 can be calculated using (1), again (unique difference is with an integral over the grating surface).

Then, (2)–(5) can be used again to obtain the final field distribution when the point defect exists. Particularly, the field distribution $E_{image}(x'', z'')$ at the image plane can be obtained by scanning over the surface of the output waveguide. Note that a repetitious scattering can occur when the diffraction field is scattered backward to the grating by the point defect. However, the repetitious scattering field is ignored in the present paper, since it is much less than the total image field.

Using above numerical model, we will analyze the scattering characteristics of a circular-hole defect located on the line from the input waveguide to the central incident point of the grating (see Fig. 5). Since the model is only 2-D, we fill the detected sample into the air circular-hole defect to simulate a sensing process (i.e., the influence of the overflowing solution on the waveguide surface is ignored). Fig. 6 shows the loss at various positions and diameters of the circular-hole defect for an EDG spectrometer at the central wavelength (i.e., 1550 nm). From this figure, one can see that some circular-hole defects with special diameters can result in very strong resonance losses. It is obvious that a larger loss can be induced when the defect is closer to the input waveguide since the intensity of the incident field is larger near the input waveguide. Moreover, the position of loss peaks is independent of the position of the defect, as the resonance only depends on the physical structure of the circular-hole defect. However, for the present sensor application, the circular-hole defect has to be placed very close to the input port (within 200 μm) to obtain enough detection sensitivity. From this figure, one also sees that there are three large (resonant) loss peaks at the range of the calculated defect diameters for the central wavelength when the defect diameter equals 0.79 μm, 2.33 μm, and 3.21 μm, respectively.

Fig. 7 shows the field distribution near the circular-hole defect with a 0.79 μm (i.e., the first resonant peak in Fig. 6) and 1.3 μm diameter, respectively. From this figure, one can see that a resonance can induce so serious departure of the incident field from the incident direction that little power can be focused into the corresponding output waveguide [see Fig. 7(a)], whereas the influence is relatively small for nonresonant case [e.g., for a defect with a 1.3-μm diameter in Fig. 7(b)].

Fig. 8 shows the calculated transmission loss around the central wavelength for above three resonant diameters (0.79 μm, 2.33 μm, and 3.21 μm) and another nonresonant (1.55 μm) diameter of the circular-hole defect. From this figure, one can see that the spectral width, which is inversely proportional to the Q factor, nonmonotonously varies at different resonance cases as the defect diameter increases. Therefore, for a given circular-hole defect, we can design the EDG spectrometer with an optimal channel interval to achieve the highest sensitivity for the present sensing application.
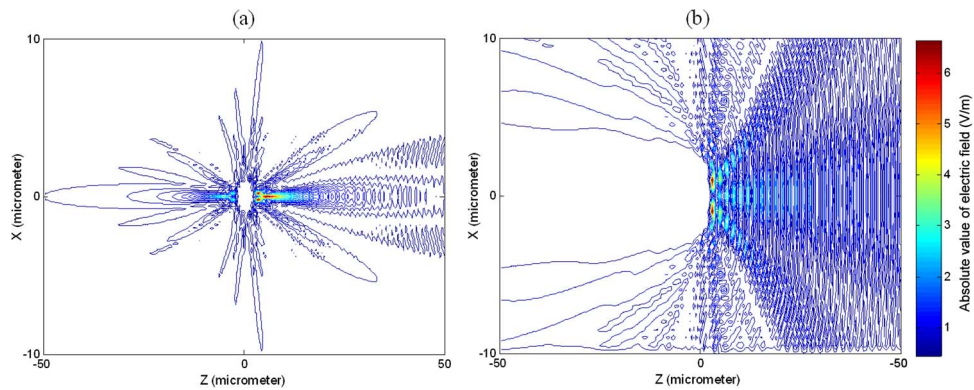
Fig. 7. Field distributions near the circular-hole defect with the 0.79 μm (a) and 1.3 μm (b) diameter at the central wavelength.
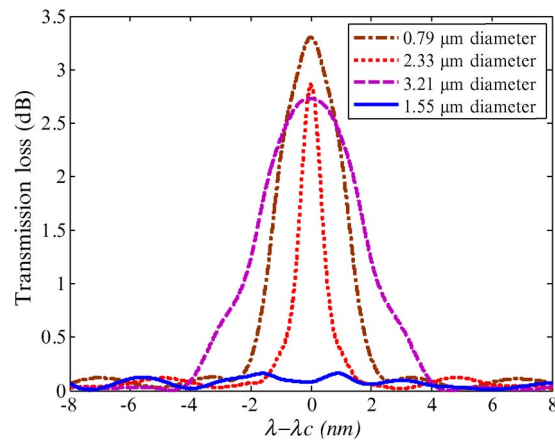

Fig. 8. Calculated transmission loss around the central wavelength for four different diameters of the circular-hole defect.
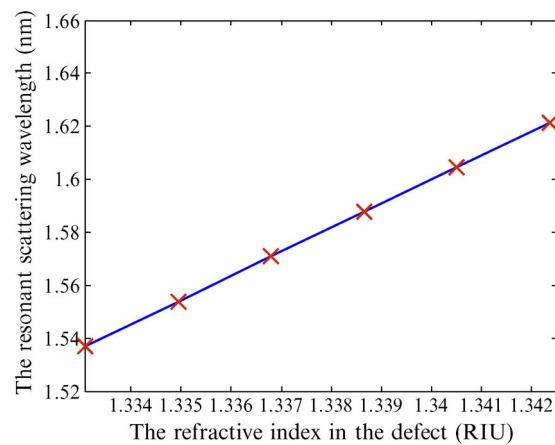

Fig. 9. Calculated resonant scattering wavelength varies as the refractive index increases.

When we fill the NaCl solution with variable concentrations from 0 to 5 mass% (i.e., refractive indices from 1.3331 to 1.3423 based on the measured relationship: $n = 1.3331 + 0.00185c\%$) into a circular-hole defect with a 1-μm diameter, we calculate that the resonant scattering wavelength varies as the refractive index increases (see Fig. 9). The numerical results agree well with the experimental values (see Fig. 4).

Note that the blazed wavelength of the EDG spectrometer without any hole defect is also sensitive to the ambient refractive due to the evanescent field sensing of the slab waveguide region. However, the sensing area is much smaller than the area of the whole FPR (see Fig. 1). As a numerical example, the evanescent field in a slab waveguide sensing region with a 10-square-micrometer area only can result in ~300 pm/RIU operating wavelength shift, which has negligible influence on the sensing device.

4. Conclusion

In the present paper, we experimentally and numerically analyzed the characteristics of an optical sensor by fabricating a circular-hole defect into the FPR of an EDG spectrometer. Numerical results indicated that we could obtain a highly sensitive sensor design when the defect was very close to the input waveguide, and furthermore, the channel interval of the EDG was appropriately chosen in terms of the defect diameter.

References

[1] T. Claes, J. G. Molera, K. De Vos, E. Schacht, R. Baets, and P. Bienstman, "Label-free biosensing with a slot-waveguide-based ring resonator in silicon on insulator," *IEEE Photon. J.*, vol. 1, no. 3, pp. 197–204, Sep. 2009.

[2] A. Densmore, M. Vachon, D. X. Xu, S. Janz, R. Ma, Y. H. Li, G. Lopinski, A. Delage, J. Lapointe, C. C. Luebbert, Q. Y. Liu, P. Cheben, and J. H. Schmid, "Silicon photonic wire biosensor array for multiplexed real-time and label-free molecular detection," *Opt. Lett.*, vol. 34, no. 23, pp. 3598–3600, Dec. 2009.

[3] E. Zinoviev Kirill, A. B. Gonzalez-Guerrero, C. Dominguez, and L. M. Lechuga, "Integrated bimodal waveguide interferometric biosensor for label-free analysis," *J. Lightwave Technol.*, vol. 29, no. 13, pp. 1926–1930, Jul. 2011.

[4] K. Q. Le and P. Bienstman, "Enhanced sensitivity of silicon-on-insulator surface plasmon interferometer with additional silicon layer," *IEEE Photon. J.*, vol. 3, no. 3, pp. 538–545, Jun. 2011.

[5] J. T. Kirk, G. E. Fridley, J. W. Chamberlain, E. D. Christensen, M. Hochberg, and D. M. Ratner, "Multiplexed inkjet functionalization of silicon photonic biosensors," *Lab on a chip*, vol. 11, no. 7, pp. 1372–1377, Jul. 2011.

[6] K. De Vos, J. Girones, T. Claes, Y. De Koninck, S. Popelka, E. Schacht, R. Baets, and P. Bienstman, "Multiplexed antibody detection with an array of silicon-on-insulator microring resonators," *IEEE Photon. J.*, vol. 1, no. 4, pp. 225–235, Oct. 2009.

[7] M. Iqbal, M. A. Gleeson, B. Spaugh, F. Tybor, W. G. Gunn, M. Hochberg, T. Baehr-Jones, R. C. Bailey, and L. C. Gunn, "Label-free biosensor arrays based on silicon ring resonators and high-speed optical scanning instrumentation," *IEEE J. Sel. Topics Quantum Electron.*, vol. 16, no. 3, pp. 654–661, May/Jun. 2010.

[8] M. S. Luchansky and R. C. Bailey, "Silicon photonic microring resonators for quantitative cytokine detection and T-cell secretion analysis," *Anal. Chem.*, vol. 82, no. 5, pp. 1975–1981, Mar. 2010.

[9] T. Claes, W. Bogaerts, and P. Bienstman, "Experimental characterization of a silicon photonic biosensor consisting of two cascaded ring resonators based on the Vernier-effect and introduction of a curve fitting method for an improved detection limit," *Opt. Exp.*, vol. 18, no. 22, pp. 22 747–22 761, Oct. 2010.

[10] T. Claes, W. Bogaerts, and P. Bienstman, "Vernier-cascade label-free biosensor with integrated arrayed waveguide grating for wavelength interrogation with low-cost broadband source," *Opt. Lett.*, vol. 36, no. 17, pp. 3320–3322, Sep. 2011.

[11] J. Song and N. Zhu, "High sensitive gas sensor application based on a small defect in silicon waveguide," *IEEE Photon. Technol. Lett.*, vol. 21, no. 1, pp. 82–84, Jan. 2009.

[12] A. Harke, M. Krause, and J. Mueller, "Low-loss single-mode amorphous silicon waveguides," *Electron. Lett.*, vol. 41, no. 25, pp. 1377–1379, Dec. 2005.

[13] M. Gnan, S. Thoms, D. S. Macintyre, R. M. De la Rue, and M. Sorel, "Fabrication of low-loss photonic wires in silicon-on-insulator using hydrogen silsesquioxane electron-beam resist," *Electron. Lett.*, vol. 44, no. 2, pp. 115–116, Jan. 2008.

[14] S. Zhu, G. Q. Lo, and D. L. Kwong, "Low-loss amorphous silicon wire waveguide for integrated photonics: Effect of fabrication process and the thermal stability," *Opt. Exp.*, vol. 18, no. 24, pp. 25 283–25 291, Nov. 2010.

[15] J. Brouckaert, G. Roelkens, D. Van Thourhout, and R. Baets, "Thin-film III–V photodetectors Integrated on silicon-on-insulator photonic ICs," *J. Lightwave Technol.*, vol. 25, no. 4, pp. 1053–1060, Apr. 2007.

[16] J. Brouckaert, W. Bogaerts, P. Dumon, J. Schrauwen, D. V. Thourhout, and R. Baets, "Planar concave grating demultiplexer fabricated on a nanophotonic silicon-on-insulator platform," *J. Lightwave Technol.*, vol. 25, no. 5, pp. 1269–1275, May 2007.

[17] J. Song and N. Zhu, "Design and fabrication of compact etched diffraction grating demultiplexers based on alpha-Si nanowire technology," *Electron. Lett.*, vol. 44, no. 13, pp. 816–818, Jun. 2008.

[18] J. Song and J. F. Ding, "Amorphous-Si-based planar grating demultiplexers with total internal reflection grooves," *Electron. Lett.*, vol. 45, no. 17, pp. 905–906, Aug. 2009.

[19] J. Song and J. F. Ding, "Analytical design of total-internal-reflection grating demultiplexers with a low noise floor," *IEEE Photon. Technol. Lett.*, vol. 22, no. 16, pp. 1229–1231, Aug. 2010.

[20] A. Jafari and A. G. Kirk, "Demonstration of distributed etched diffraction grating demultiplexer," *IEEE Photon. J.*, vol. 3, no. 4, pp. 651–657, Aug. 2011.

[21] J. Song, X. Zhou, Y. Li, and X. Li, "Planar grating demultiplexers using silicon nanowire technology with flat passband and low crosstalk," *Electron. Lett.*, vol. 47, no. 22, pp. 1241–1243, Oct. 2011.

[22] P. Debackere, R. Baets, and P. Bienstman, "Bulk sensing experiments using a surface-plasmon interferometer," *Opt. Lett.*, vol. 34, no. 18, pp. 2858–2860, Sep. 2009.

[23] G. H. Goedecke and S. G. O'Brien, "Scattering by irregular inhomogeneous particles via the digitized Green's function algorithm," *Appl. Opt.*, vol. 27, no. 12, pp. 2431–2438, Jun. 1988.